Nanophotonics and near field / Nanophotonique et champ proche

Uncovering phase maps from surface plasmon resonance images: Towards a sub-wavelength resolution

Extrayant les cartes de phase d'images à résonance plasmonique : vers une résolution sous-longueur d'onde

Françoise Argoul [a,b,*], Thibault Roland [a,b], Audrey Fahys [a,b], Lotfi Berguiga [a,b], Juan Elezgaray [c]

[a] *Université de Lyon, 69000 Lyon, France*
[b] *USR3010 laboratoire Joliot-Curie, UMR5672 laboratoire de physique, CNRS, Université de Lyon, Ecole normale supérieure de Lyon, 46, allée d'Italie, 69364 Lyon, France*
[c] *UMR5248 CNRS, université Bordeaux 1, ENITAB, IECB, 2, rue Robert-Escarpit, 33607 Pessac, France*

ARTICLE INFO

ABSTRACT

We present an original method for uncovering phase maps from surface plasmon resonance microscopy images. The phase images obtained from the recording of $V(Z)$ maps with a scanning surface plasmon microscope are affected by zero-mean uncorrelated noise and mechanical drifts. We propose to replace standard phase unwrapping methods by the computation of the local derivative of the phase $\Delta\phi/\Delta Z$ from the $V(Z)$ complex field. Phase unwrapping basically relies on a smoothness constraint of the phase field, which is severely hampered by the noise. Applications of the proposed derivation to interferometric plasmon phase images demonstrate a superior ability of restoring phase maps, preserving their discontinuities, together with an effective noise smoothing performance, irrespective of locally varying coherence characteristics.

© 2012 Académie des sciences. Published by Elsevier Masson SAS. All rights reserved.

RÉSUMÉ

Nous proposons une méthode originale pour extraire les cartes de phase d'images obtenues par microscopie à résonance plasmonique. Les images de phases recalculées à partir des cartes $V(Z)$ complexes incluent également les composantes de bruit et de dérive mécanique, ce qui rend leur déroulement difficile. Nous proposons ici de remplacer les méthodes de déroulement de la phase par le calcul de la dérivée locale $\Delta\phi/\Delta Z$ de cette phase à partir du champ complexe $V(Z)$. Cette méthode de dérivation directe à partir du champ complexe $V(Z)$ s'avère beaucoup plus efficace pour restaurer les discontinuités de la phase et permettre également un lissage plus performant du bruit, indépendamment des caractéristiques locales de la cohérence du champ électrique réfléchi après excitation du plasmon de surface.

© 2012 Académie des sciences. Published by Elsevier Masson SAS. All rights reserved.

* Corresponding author at: UMR5672 laboratoire de physique, CNRS, Ecole normale supérieure de Lyon, 46, allée d'Italie, 69364 Lyon, France.
E-mail address: francoise.argoul@ens-lyon.fr (F. Argoul).

1. Introduction

Surface plasmon resonance (SPR) is characterized by a sharp drop of the reflectivity intensity near a resonance angle (Θ_p). This effect has been extensively used for more than two decades to probe minute index variations at the interface between a gold film and a dielectric medium [1–3]. In their simplest form, SPR reflectivity measurements have been used to detect molecular adsorption, such as polymers, DNA or proteins, self-assembled layers,... [4–6]. The mechanism of SPR detection is based on the modification of the plasmon resonance by a local refractive index gradient induced by the adsorption of molecules close to the gold interface. The plasmon wave undergoes a modification of both its amplitude and its phase when it meets an obstacle of different index.

It has been shown by ellipsometry [7] that the sharp drop in SPR reflectivity is accompanied by a very fast jump in the angular dependence of the phase ϕ of the reflected beam. However, this method was not much developed afterwards because it complicated real-time diagnostics. Interferometric methods were investigated to extract the phase of the SPR in the mid nineties [8,9]. Coupling an interferometer to a SPR system, Kabashin and Nikitin predicted a sensitivity threshold ($\Delta n \sim 4 \times 10^{-8}$ RIU), two orders of magnitude smaller than SPR angular shift measurement methods. Thanks to these experiments they concluded to the possibility to improve the sensitivity of SPR systems [10,11]. More recently, other experimental studies performed also with an SPR interferometer provided a refractive index measurement sensitivity of $\Delta n \sim 3 \times 10^{-6}$ RIU, comparable to the value reported for reflectivity-based SPR systems. This limitation was imputed to the difficulty of controlling the angle of incidence [12,13].

Quite simultaneously, a new generation of Interferometric SPR Imaging (ISPRI) systems was proposed to reconstruct SPR phase images [14,15]. The system of Grigorenko and coworkers [14] could work either in a Zernike mode for phase contrast, or in the fringe mode, or finally in a conventional amplitude SPR microscope, by occulting the reference beam of the interferometer. Although enhanced sensitivity and higher resolution over conventional SPR microscopy were achieved with ISPRI, the spatial resolution remained much larger than the wavelength due to the lateral propagation of the plasmon [16,17]. More recently, a dark-field variant of this system was proposed by this group to improve the contrast [18]. Other groups have also invested much instrumentation efforts in developing ISPRI systems [19,20] and pushing down its sensitivity to $\lesssim 10^{-5}$ RIU.

A drastic gain in the lateral resolution of SPR imaging [21] was achieved by the replacement of the coupling prism by a high numerical aperture objective lens to launch the plasmon waves [22–24]. Photon scanning tunneling techniques were also applied [25,26] to capture the near-field amplitude signal and characterize the SP propagation on the scale of a few tens of nanometers. These methods were very important to confirm that prism-coupled SPR imaging cannot achieve a sub-wavelength resolution due to the lateral propagation of the surface plasmon waves [16,17]. The possibility of reconstruction of sub-wavelength resolution maps of propagating surface plasmon with a far-field microscope was demonstrated by Somekh and coworkers, both experimentally and theoretically [23,24,27]. Subsequent high resolution SPR microscopy methods constructed around a high numerical aperture objective lens concentrated exclusively on amplitude images, and did not discuss the possibility of high resolution SPR phase imaging with a far-field microscope [28–32].

The scanning surface plasmon microscope (SSPM) that is discussed here is a combination of a heterodyne interferometer, a high numerical aperture objective lens and a three-dimensional scanning device. These three points confer to this system an original ability to measure the Z derivative of the phase of the $V(Z)$ curves: $\Delta\Phi/dZ$ that none of the other systems did afford previously. We show that this derivative $\Delta\Phi/dZ$, in a very similar way to the SPR phase ϕ, crosses singular points at precise values of Z. These focus positions Z correspond to highly contrasted reconstructed images, which increases the sensitivity of SPR imaging systems.

2. Surface plasmon resonance: from intensity to phase detection

2.1. Introduction to surface plasmon resonance

The most common approach to surface plasmon excitation is to monitor the wave vector component normal to the gold interface in attenuated total reflection (ATR), thanks to a prism coupler. Two configurations have been proposed, respectively the Kretschmann geometry [33] and the Otto geometry [1]. In the Kretschmann geometry a prism with refractive index n_c is covered by a metal–dielectric waveguide consisting of a thin metal film (with permittivity $\varepsilon_m = \varepsilon_m' + i\varepsilon_m''$) and thickness δ, and a semi-infinite dielectric medium with a refractive index n_D. When a light wave is propagated through the prism, incidently to the metal film interface, a part of it is reflected back into the prism and the other part propagates in the metal/dielectric interface, in the form of an attenuated wave on both sides of the metal/dielectric interface. The propagation constant (k_{SP}) for surface plasmon in a Kretschmann configuration can be written

$$k_{SP} = \frac{\omega}{c}\sqrt{\frac{\varepsilon_D \varepsilon_m}{\varepsilon_D + \varepsilon_m}} + \Delta k$$

The first term is the propagation constant of the surface plasmon metal–dielectric waveguide without the prism, and Δk accounts for the prism coupling condition, that produces the evanescent wave. For the plasmon resonance to occur, the

propagation constant k_{EW} of the evanescent wave and that of the surface plasmon k_{SP} must be equal along the propagation direction (x):

$$k_{EW} = \frac{\omega}{c} n_c \sin\theta = k_{SP} = k'_{SP} + i k''_{SP}$$

The fact that k_{SP} is parallel to the gold interface imposes that the incident electric field is **p**-polarized (transverse mode (TM) for the magnetic field). For each wavelength, the matching condition for SPR is fulfilled for a single angle of incidence θ_P, the coupling angle, which increases with a decreasing wavelength. The lateral propagation length L_x of the plasmon wave is directly related to the inverse of the imaginary part of k_{SP}: $L_x = 1/2k''_{SP}$. If one neglects in a first approximation the correction of k_{SP} due to the prism coupler (Δk) the lateral propagation length behaves as:

$$L_x = \frac{1}{2k''_{SP}} = \frac{\omega}{c} \left\{ \frac{\varepsilon'_m + \varepsilon_D}{\varepsilon'_m \varepsilon_D} \right\}^{3/2} \frac{\varepsilon'^{\,2}_m}{\varepsilon''_m}$$

In the case of a gold metal film in contact with air, the real part of ε is very large and negative. Therefore L_x can be approximated by: $L_x \simeq \{\omega/c\} \varepsilon'^2_m / \varepsilon''_m$, for $\lambda = 633$ nm, $L_x \simeq 10$ μm, which explains the low resolution achieved by prism-coupled ISPRI microscopies presented in the introduction [14,15,19,20]. As a consequence, it is necessary to confine and to partially localize either the measuring probe (scanning probe of a near-field microscope) or the excitation system (high numerical aperture objective lens) to go beyond this limitation. The second method will be discussed in Section 3.

2.1.1. Evanescent waves

Evanescent waves occuring for angles of incidence greater than the critical angle θ_C are described by a penetration depth which quantifies the confinement of the field in the vicinity of the interface. This penetration depth depends on the indices of the two media bounding the interface, for instance the index of glass n_c and the index of the dielectric medium n_D [34]:

$$l_z = \frac{\lambda}{2\pi \sqrt{n_c^2 \sin^2\theta - n_D^2}}$$

When the angle of the incident beam θ increases from θ_C to $\pi/2$, l_z decreases from ∞ to $l_{zm} = \frac{\lambda}{2\pi\sqrt{n_c^2 - n_D^2}}$. In practice for a glass/air interface, and 633 nm wavelength, $l_{zm} \sim 140$ nm when $\theta \to \pi/2$. When SPR is involved, at θ_P, the penetration depth is larger than l_{zm} in the dielectric medium:

$$l_{z^{SP}} = \frac{\lambda}{2\pi} \left\{ \frac{|\varepsilon'_m + \varepsilon_D|}{\varepsilon_D^2} \right\}^{1/2}$$

z is the direction normal to the gold interface. If we consider the permittivity of gold at 633 nm: $\varepsilon_m = -11.8134 + 1.2144i$, we get $l_{z^{SP}} \sim 331$ nm.

2.1.2. The surface plasmon resonance

In Kretschmann configuration, SPR depends on several parameters, the most commonly studied being for instance the angle of incidence, the wavelength of the excitation beam and its polarization, the gold film index and thickness and the index distribution of the dielectric medium in contact with gold [35]. As suggested by Raether [36], SPR depends also on the gold roughness and we have also shown recently that thin gold films prepared by thermal evaporation have both a gold surface roughness and an internal lacunarity which influence SPR conditions of excitation [37,38]. When SPR is tuned near its reflectivity minimum, the phase of the plasmon undergoes an abrupt change which depends also on the same parameters as given above [11].

2.2. Evolution of the SPR curves with gold film thickness

We make a comparative analysis in this section of the influence of the gold film thickness on SPR intensity and phase curves in **s** and **p** polarizations. We conclude from Fig. 1 that the thickness of the gold film has a strong influence on the plasmon resonance (in **p** polarization) intensity and phase reflectivity curves.

We note in Fig. 1 that the sharpest drop is obtained in this computation for a thickness of gold close to 38 nm, where the phase drop is about -2π at the angle of resonance. This thickness corresponds also to the sharpest drop of the reflected intensity in **p** polarization. Above this value, the phase drop at resonance decreases, and its sign of variation changes also at the resonance. Therefore, around 38 nm, a minute change in gold thickness induces a reversal of the phase drop at resonance, which can be interpreted as a phase singularity since the reflection at resonance tends to zero. Therefore, both the gold thickness and index may be adjusted to narrow the range of the phase jump at the resonance [11].
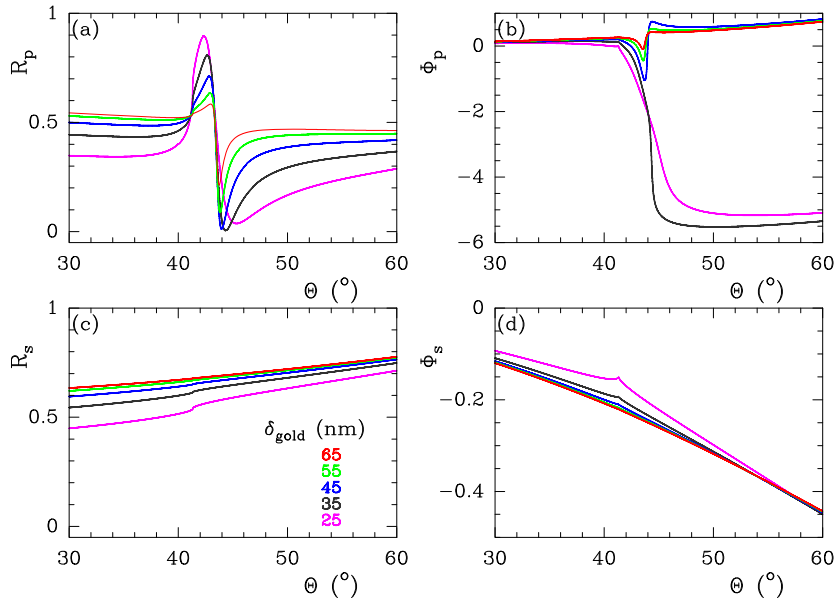
Fig. 1. Evolution of the SPR intensity and phase curves with the thickness of the gold film. (a) $R_p = |r_p|^2$ versus θ. (b) ϕ_p versus θ. (c) $R_s = |r_s|^2$ versus θ. (d) ϕ_s versus θ. Wavelength $\lambda = 633$ nm, the dielectric constants of gold and chromium (adhesion layer for gold) are $\varepsilon_{Au} = -11.81 + 1.214i$, $\varepsilon_{Cr} = -1.1125 + 20.793i$, $\delta_{Cr} = 5$ nm.

2.3. Interferometric SPR phase measurement

It was shown by Abeles and coworkers [7] in the early seventies that SPR phase can be measured by ellipsometry. However, interferometric techniques were rapidly preferred because they are more effective to discriminate the signal from the background noise. As already reported in the introduction, several groups have proposed different interferometric setups to measure the plasmon phase drop at resonance [8–13,39].

The extension of these interferometric set-ups to ISPRI systems was a natural consequence and exploitation of the previously developed experimental skills in SPR experimentations [14,15,18–20]. Despite the fact that these set-ups were offering improved sensitivity, their spatial resolution was definitely limited by the intrinsic nature of the plasmon wave, i.e. its propagative nature parallel to the plane of gold surface (k_x), and the fact that the propagation length in this direction is greater than the excitation wavelength (see Section 2.1).

## 3. The scanning surface plasmon microscopy: SSPM

A drastic gain in SPR imaging lateral resolution was achieved, by replacing the coupling prism with a high aperture objective lens to launch the plasmon [22–24]. Sub-wavelength resolution SPR imaging was recently applied to nanometer size colloid imaging [40]. All the studies performed afterwards on SPR high resolution microscopy constructed around a high numerical aperture objective lens concentrated exclusively on amplitude images, and did not discuss the possibility of high resolution SPR phase imaging with a far-field microscope [28–32]. We propose here to reconstruct plasmon phase images.

3.1. Presentation of the SSPM

The scanning surface plasmon microscope (SSPM) combines in a single apparatus several advantages, and we want to demonstrate also that it allows measurements of the Z derivative of the plasmon phase that none of the ISPRI systems already mentioned in the introduction could afford.

This high resolution microscopy method is different from standard SPR imaging methods for several reasons which are listed below. It includes:

- Focusing of light by a high numerical aperture (NA) objective lens;
- Polarization of light (radial, azimuthal, linear);
- Interferometric heterodyne detection to capture the back reflected field, integrated over the objective pupil, and remove the background noise for higher signal to noise ratio;
- Scanning in (X, Y) and Z directions: for fixed Z, 2D images in (X, Y) plane are reconstructed; for fixed (X, Y), $V(Z)$ curves are recorded by varying the focus position Z. $V(Z)$ curves model the variation of the integral of the back reflected beam over the objective pupil versus the distance Z of the objective lens focus point to the gold interface;
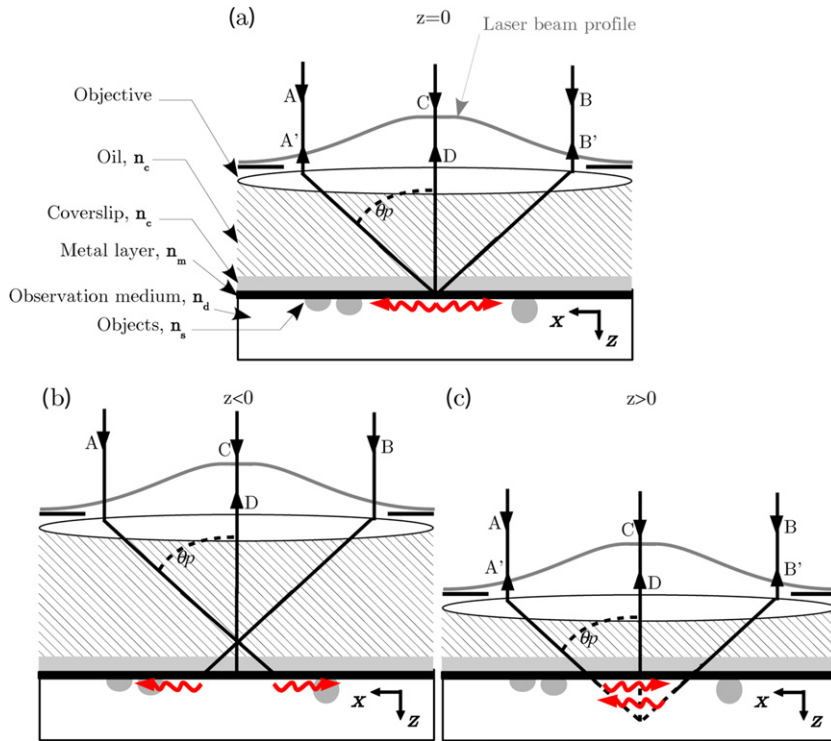
Fig. 2. SSPM principle of light coupling for surface plasmon excitation. A Gaussian shaped laser passes through a high NA objective lens and launches the surface plasmon wave (depicted as red ripples) for the incident ray angle corresponding to θ_P. A', B' and D represent the back reflected rays, and A, B and C the corresponding incoming rays. The objective is (a) at focus $Z = 0$, (b) defocalized in the coupling medium $Z < 0$, and (c) in the observation medium $Z > 0$.

- Conditioning of the incoming light to enhance SSPM sensitivity, for instance by a diaphragm that increases the fraction of light that contributes to SPR excitation.

3.1.1. SSPM set-up

The experimental device allowing radial and azimuthal polarization of high resolution surface plasmon imaging has already been reported in Refs. [41,42]. Fig. 2 sketches the objective lens, the glass coverslip and its metal coating (5 nm chromium and 45 nm gold) and the incoming and exiting light beams. At focus ($Z = 0$) (Fig. 2(a)) and out of focus ($Z > 0$) (Fig. 2(c)) the incoming rays (A) reradiate in rays (B') that contain amplitude and phase information about SP propagation inside the confined area. When the focus is located in the coupling medium ($Z < 0$) (Fig. 2(b)) surface plasmon waves propagate outwards the focal spot and do not contribute to the image contrast. Therefore, the radial symmetry of the high NA objective lens produces a confinement of the SP waves in a very small zone. The rays (C) which are not coupled to SP are reflected back (D) without SP phase retardation.

3.2. $V(Z)$ curves: defocusing the objective lens enhances contrast

When the objective lens is scanned along its axis (Z), a $V(Z)$ signal is recorded on the photomultiplier. The measurement of this function versus the distance of the objective lens focal point to the gold surface (Z) is at the basis of SSPM image contrast. This method is directly inspired from scanning acoustic microscopy [43,44,23].

$$V(Z) = \int_{\theta_{min}}^{\theta_{max}} P^2(\sin\theta)\mathcal{Q}(\theta)\exp(2jkn_cZ\cos\theta)\cos\theta\sin\theta\,d\theta \qquad (1)$$

where P is the pupil function of the objective lens, n_c is the index of the coupling medium (lens and matching index oil), k the wave number, $\mathcal{Q}(\theta)$ is proportional to the back reflected field, integrated over the radial angle φ. This quantity depends on the light polarisation, for **p** polarised light it reads

$$\mathcal{Q}(\theta) = \int_0^{2\pi} -r_p(\sin\theta)\cos^2\varphi\,d\varphi = -\pi r_p(\sin\theta)$$
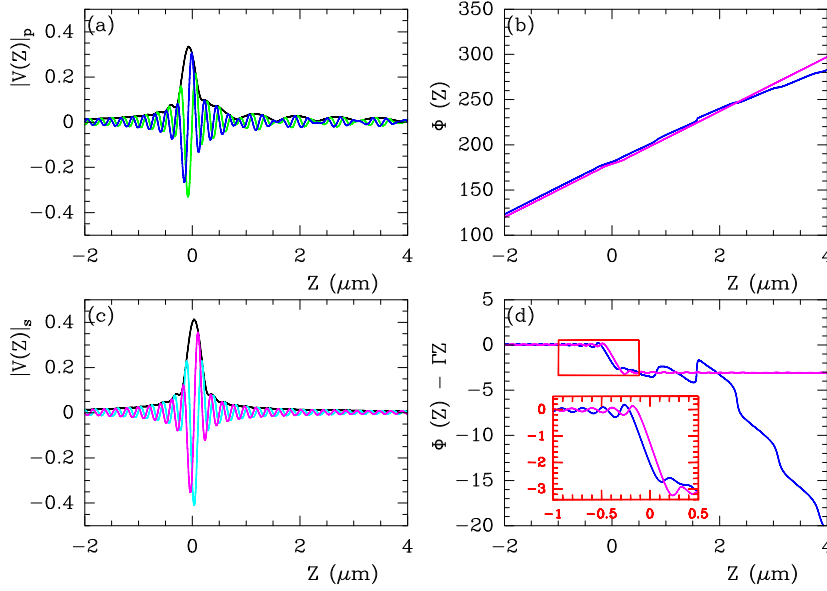
Fig. 3. Theoretical $V(Z)$ curves illustrating the SSPM response of a thin gold film in air. (a) $|V(Z)|$ (black), $\Re(V(Z))$ (green) and $\Im(V(Z))$ (blue) in **p** polarization mode. (b) Unwrapped phase Φ of $V(Z)$ in **p** (blue) and **s** (magenta) polarization modes respectively. (c) $|V(Z)|$ (black), $\Re(V(Z))$ (cyan) and $\Im(V(Z))$ (magenta) in **s** polarization mode. (d) Corrected phase ($\Phi - \Gamma Z$) by a linear trend with slope Γ estimated by a linear fitting each $V(Z)$ curve for $Z < 1$ μm. $\lambda = 633$ nm, $\varepsilon_{Au} = -11.81 + 1.214i$, $\delta_{Au} = 45$ nm, $\varepsilon_{Cr} = -1.1125 + 20.793i$, $\delta_{Cr} = 5$ nm.

for **s** polarized light:

$$Q(\theta) = \int\limits_0^{2\pi} r_s(\sin\theta) \sin^2\varphi \, d\varphi = \pi r_s(\sin\theta)$$

The $V(Z)$ curve is a Fourier transform of the reflected field with the change of variable [45]:

$$\nu = 2kn_c \cos\theta; \qquad d\nu = -2kn_c \sin\theta \, d\theta$$

Therefore $V(Z)$ reads

$$V(Z) = \frac{1}{4k^2 n_c^2} \int\limits_{\nu_{\min}}^{\nu_{\max}} P^2(\nu/k) Q(\nu/k) \exp(j\nu Z) \nu \, d\nu \qquad (2)$$

For an objective lens with numerical aperture NA, $\theta_{\max} = \arcsin(\text{NA}/n_c)$ and $\nu_{\min} = 2kn_c\sqrt{1 - \text{NA}^2/n_c^2}$. Without any diaphragm of the light, we have $\theta_{\min} = 0$, and $\nu_{\max} = 2kn_c$. By putting the pupil function P equal to zero outside the angular interval [$\theta_{\min} = 0, \theta_{\max}$], on gets an integral in the infinite domain for ν:

$$V(Z) = \frac{1}{4k^2 n_c^2} \int\limits_{-\infty}^{\infty} P^2(\nu/k) Q(\nu/k) \exp(j\nu Z) \nu \, d\nu \qquad (3)$$

If the reflection of light is homogeneous on the angular domain of the optical system, the integral $V(Z)$ corresponds to the Fourier transform of a linear function in the [$\nu_{\min}, \nu_{\max}$] domain.

3.3. Modulus and phase of $V(Z)$

This $V(Z)$ function is a complex quantity and we can therefore plot its modulus, but also its real and imaginary parts, as shown in Figs. 3(a) and 3(c) for **p** and **s** polarizations respectively. Here we consider a 45 nm thick gold film with a 5 nm chromium sublayer, and a 633 nm wavelength. The difference of the two $|V(Z)|$ curves, respectively for a **p** and a **s** polarization, is stronger for positive values of Z that correspond to a focusing inside the dielectric (air) layer in contact with the gold interface. Slow oscillations, characteristic of plasmon resonance for **p** polarization, superimpose on the $|V(Z)|$ curves. Their period can be approximated by the equation $\Delta Z_{SP} = \lambda/2n_c(1 - \cos\theta_P)$ [24], with n_c the index of glass, θ_P the

angle of plasmon resonance ($\simeq 44°$, see Fig. 1), which gives in our example: 744 nm. This modulation is not observed for **s** polarization.

The real $\Re(V(Z))$ and imaginary $\Im(V(Z))$ parts of $V(Z)$ are oscillating functions of Z. Their frequency can be approximated by the factor which appears in the exponential term of $V(Z)$ (Eq. (1)): $2kn_c = 4\pi n_c/\lambda$, with a mean period of $f_m = \lambda/2n_c \sim 210$ nm. These oscillations of $\Re(V(Z))$ and $\Im(V(Z))$ are not purely harmonic, since their phase Φ is not a pure linear function of Z, as could be expected if the reflectivity r_p of the interface was real and equal to unity. The fact that r_p is a complex quantity, with a phase depending on the angle of incidence θ, is directly translated in the way the phase Φ of $V(Z)$ changes with Z.

From a practical point of view, our aim here is to extract this phase from numerical and experimental data and to pave the way for interpreting the $\Phi(Z)$ curves. We propose therefore to revisit phase computation methods applied to $V(Z)$ curves and to explain how phase extraction can be improved in our case.

3.4. Computation of the phase from the $V(Z)$ curves

A standard method to extract the phase from a complex quantity such as $V(Z)$ is to compute its argument Φ, thanks to the arctangent of the ratio $\Im(V(Z))/\Re(V(Z))$. This argument is then unwrapped to recover from artificial discontinuities due to the arctangent function. This method is illustrated in Fig. 3, where we compare this computation for **p** and **s** polarizations. The phase increases with the variable Z, and if the surface reflectance was flat ($r_p = 1, \forall\theta$) it would be a linear function. $V(Z)$ can be written as

$$V(Z) = |V(Z)| \exp(i\Phi(Z))$$

with $\Phi(Z)$ the phase of $V(Z)$. Fig. 3(d) shows that if one substracts a linear function of Z to $\Phi(Z)$, the corrected Φ curve does not behave as a simple harmonic form when SPR is excited. Γ is estimated by a least square deviation fitting of $\Phi(Z)$ in Fig. 3(b) in the Z interval $[-6\ \mu m; -1\ \mu m]$. This representation shows that both $\Phi(Z) - \Gamma Z$ curves present a phase drop of π close to $Z = 0$, independently from the polarization. This phase drop is shifted towards positive value of Z by about 100 nm when the polarization is switched from **p** to **s**. In **s** polarisation, beyond this π phase drop close to the origin of Z, the phase recovers a quasi-linear behavior for positive values of Z. In **p** polarization, the phase remains in the neighbourhood of the linear ΓZ function below 2 μm, but beyond 2 μm, it adopts a nonlinear behavior.

We conclude from this illustration that it is difficult from the plot of Φ to get a correct interpretation of the evolution of the phase for positive values of Z, if surface plasmon resonance is involved. Experimentally, the level of noise can be relatively important in such a way that the computation of arctangent is unstable when the real part of $V(Z)$ crosses zero.

All these aspects pushed us to consider another method to exploit the phase of $V(Z)$, inspired from dynamical systems. Actually, if one takes Z as a dynamical variable, the complex quantity $V(Z)$ can be treated as a dynamical variable, with a modulus describing the scalar response of the system, and a phase describing the damping of the system. A three-dimensional (3D) representation of $V(Z)$ illustrates this analogy (see Fig. 4). The black trajectory corresponds to the modulus of $V(Z)$ that presents a spiral shape, shrinked at both ends (large Z values). When Z changes, the system visits this trajectory with a velocity which can be computed from the gradients of $[\Re(V(Z)), \Im(V(Z))]$. This velocity has been normalized by $|V(Z)|$ at each position Z, and depicted as a red arrow. Comparison of the **p** velocity map in Fig. 4(b) with the **s** velocity map in (a) gives a direct clue of the influence of SPR on the phase of $V(Z)$. The angular velocity of the $V(Z)$ vector field increases rapidly when the modulus of $V(Z)$ approaches zero, reminding us of the way the SPR reflectivity phase drops also very sharply at the resonance angle θ_P (see Fig. 1).

Below this 3D representation of Fig. 4, we plot the derivative of Φ versus Z, in radian/μm, for **s** (c) and **p** (d) polarization respectively in the interval $[-6\ \mu m, 6\ \mu m]$. For **p** polarization, we note another interesting phenomenon: after two sharp accelerations of the phase velocity below $Z = 2$ μm, at the next minimum of $|V(Z)|$ this velocity has unexpectedly slowed down. However, this effect looses progressively its strength when Z increases. Again, this reversal of the phase velocity variations reminds us that the SPR phase shows also a reversing close to θ_P (see Fig. 1). This reversal process is also shown with the $V(Z)$ curve when defocusing inside the dielectric medium.

3.5. Influence of the gold thickness on the $V(Z)$ curve

In a similar manner as SPR phase curves, the reversing process presented in the previous paragraph with the $\Delta\Phi/\Delta Z$ curves depends on the thickness of the gold layer too. We have seen in Fig. 1 that for a thickness below 38 nm, the SPR phase decreases monotonously, whereas above 38 nm, it presents a minimum value for θ_P. For the same set of parameters as in Fig. 5, we have computed the behavior for both the modulus and the derivative of the phase of $V(Z)$, for pure **p** (radial) and pure **s** (azimuthal) polarization while varying the thickness of the gold layer.

3.6. $V(Z)$ response depends mostly on the SPR phase

Phase variations of r_p at resonance have a strong influence not only on the phase of $V(Z)$ but also on the modulus of the $V(Z)$ [46]. In Fig. 6 we have put the modulus of r_p and r_s equal to 1 to consider only their phase variation in θ in the
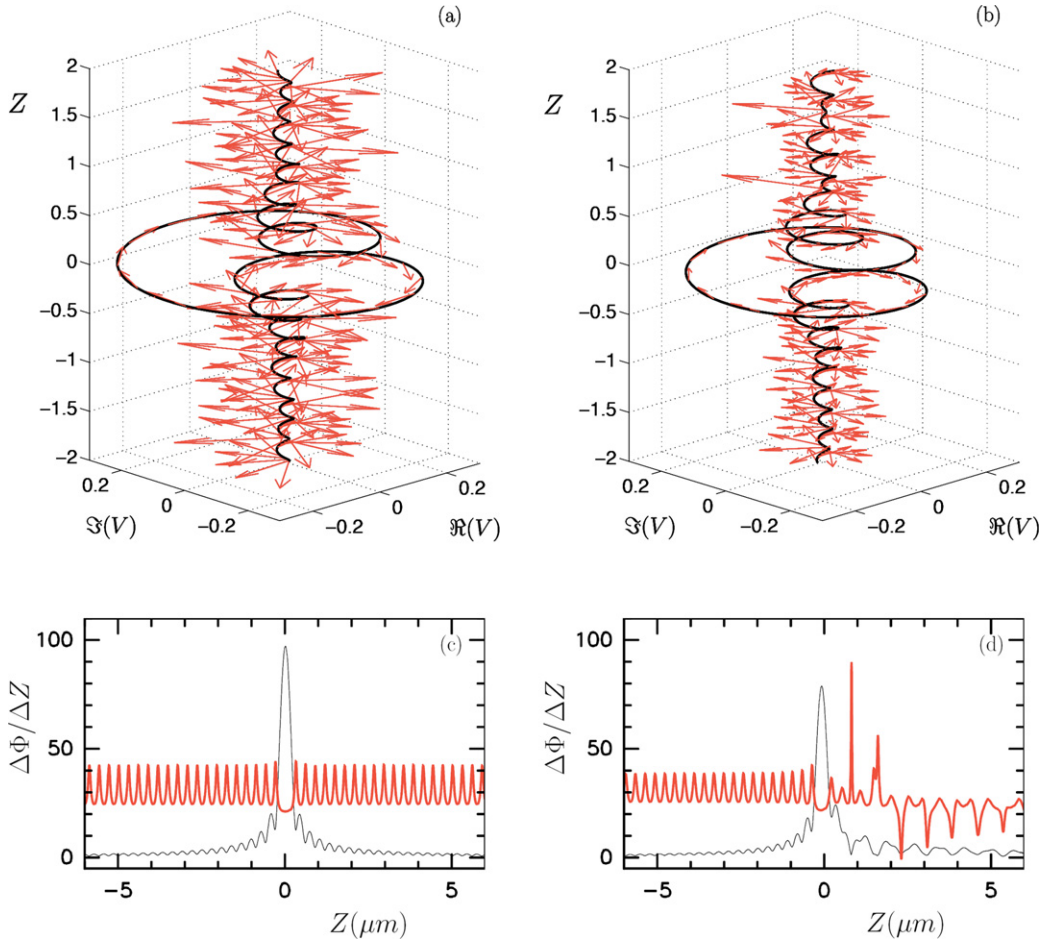
Fig. 4. 3D representation of $V(Z)$. (a) **s** polarization mode. (b) **p** polarization mode. (c) $\Delta\Phi/\Delta Z$ in **s** polarisation (red). (d) $\Delta\Phi/\Delta Z$ in **p** polarisation (red). The corresponding $|V(Z)|$ plots are superimposed in (c) and (d) for convenience. $\lambda = 633$ nm, $\varepsilon_{Au} = -11.81 + 1.214i$, $\delta_{Au} = 45$ nm, $\varepsilon_{Cr} = -1.1125 + 20.793i$, $\delta_{Cr} = 5$ nm.

computation of the integral $V(Z)$. Obviously, the amplitude of $V(Z)$ increases globally, since the intensity attenuation due to gold layer is cancelled. The remarkable phenomenon illustrated here is that the slow amplitude modulations corresponding to SPR in **p** polarization are rather amplified than damped. The phase derivative $\Delta\Phi/\Delta Z$ still shows singularities in Z. However, we note also that the strength of these singularities is increased for a thickness lower than 50 nm, whereas it is decreased for thicknesses larger than 50 nm. The interplay of amplitude and phase of r_p adds a second order correction for the phase of $V(Z)$.

### 3.6.1. Role of diaphragming the objective lens

We consider in this section the limitation of incidence angle aperture by the objective lens, and the modification of the $V(Z)$ that it entails. As an illustration, we consider an objective lens with $NA = 1.45$ that we use in air. The maximum angle for the integration of $V(Z)$ is therefore: $\theta_{max} = \mathrm{asin}(NA/n_c) = 73.14°$, $n_c = 1.51$.

We observe in Fig. 7 that diaphragming the angles of incidence increases the lateral modulations of $|V(Z)|$ for **s** and **p** polarizations. Although these small amplitude modulations superimpose to the slower plasmon $V(Z)$ modulations for $Z > 0$ in Fig. 7(a), their discrimination from plasmon oscillations is still possible. We note also that for **s** polarisation the modulations change slightly with the thickness of gold film, however, the modification of the slower $V(Z)$ modulations with gold thickness is much greater. These differences are more obvious when comparing the derivative of $\Phi(Z)$ phase (Figs. 7(b) and 7(d)). For **s** polarization we observe a strong amplification of the fast modulations of $\Delta\Phi_S/\Delta Z$ for both positive and negative values of Z. For **p** polarization this amplification of the fast $\Delta\Phi_S/\Delta Z$ modulations still exists for negative values of Z, whereas for positive values of Z they are damped and overwhelmed by the slower modulations of $\Delta\Phi_S/\Delta Z$ due to plasmon resonance effect. Again, we note that the peaks of $\Delta\Phi_S/\Delta Z$ can be reversed, and that this reversal depends still on the thickness of the gold layer.
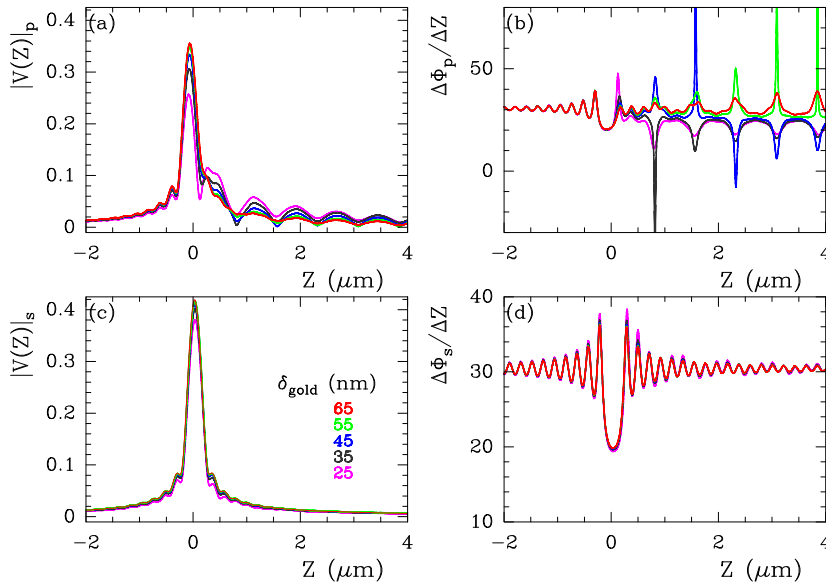
Fig. 5. Evolution of the modulus $|V(Z)|$ and the derivative of the phase $\Delta\Phi/\Delta Z$ of the complex $V(Z)$ curves as a function of the gold film thickness. (a) $|V(Z)|_p$ versus Z. (b) $\Delta\Phi_p/\Delta Z$ versus Z. (c) $|V(Z)|_s$ versus Z. (d) $\Delta\Phi_s/\Delta Z$ versus Z. $\lambda = 633$ nm, $\varepsilon_{Au} = -11.81 + 1.214i$, $\delta_{Au} = 45$ nm, $\varepsilon_{Cr} = -1.1125 + 20.793i$, $\delta_{Cr} = 5$ nm.
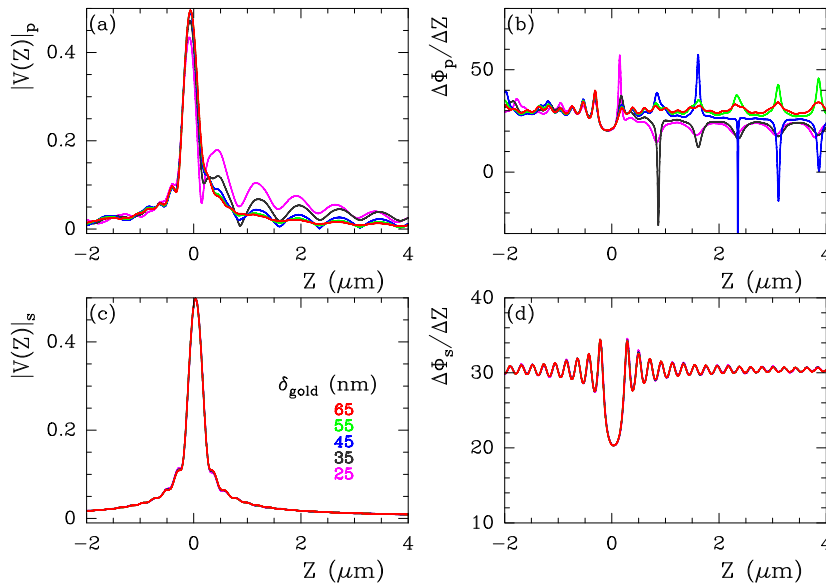

Fig. 6. $V(Z)$ curves computed from pure phase variation of r_p and r_s, corresponding to Fig. 5. The modulus of r_p and r has been arbitrarily put to 1 and the $V(Z)$ recalculated. (a) $|V(Z)|_p$ versus Z. (b) $\Delta\Phi_p/\Delta Z$ versus Z. (c) $|V(Z)|_s$ versus Z. (d) $\Delta\Phi_s/\Delta Z$ versus Z. $\lambda = 633$ nm, $\varepsilon_{Au} = -11.81 + 1.214i$, $\delta_{Au} = 45$ nm, $\varepsilon_{Cr} = -1.1125 + 20.793i$, $\delta_{Cr} = 5$ nm.

4. Application to a patterned gold surface

4.1. Preparation of the patterned gold surface

To illustrate our theoretical discussion of surface plasmon phase imaging, we have chosen a structured gold sample, prepared by I. Roch Jeune at IEMN (UMR CNRS 8520, Villeneuve d'Ascq, France). Electron-beam lithography and lift-off process were used to define a Ti:Au patterned surface, with square holes milled inside the gold layer. After depositing the Ti:Au (5 nm:45 nm) layer on a glass coverslip, a positive resin is deposited on the gold layer. The electron beam is used to write the area of the sample where gold will be etched by an ion beam. In a last step the resin layer is removed by
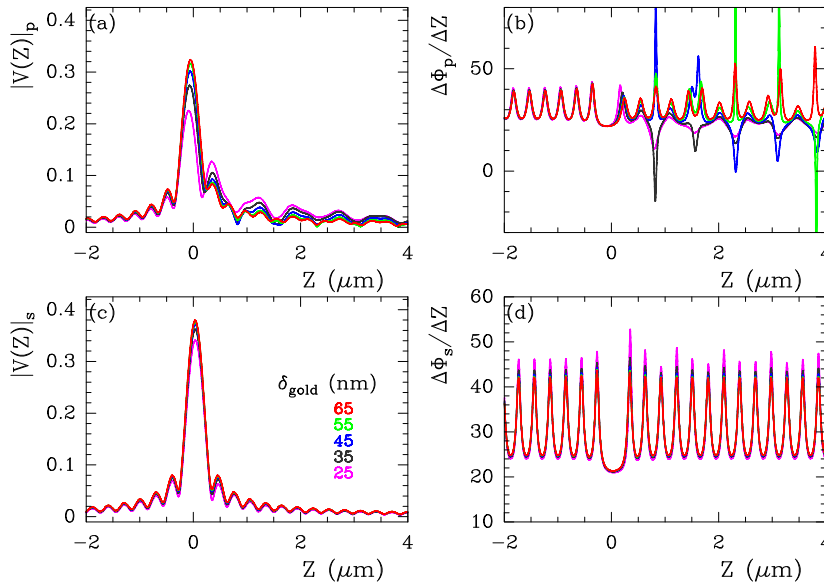
Fig. 7. Evolution of the modulus $|V(Z)|$ and the derivative of the phase $\Delta\Phi/\Delta Z$ of the complex $V(Z)$ curves with the gold film thickness. (a) $|V(Z)|_p$ versus Z. (b) $\Delta\Phi_p/\Delta Z$ versus Z. (c) $|V(Z)|_s$ versus Z. (d) $\Delta\Phi_s/\Delta Z$ versus Z. $\lambda = 633$ nm, $\varepsilon_{Au} = -11.81 + 1.214i$, $\delta_{Au} = 45$ nm, $\varepsilon_{Cr} = -1.1125 + 20.793i$, $\delta_{Cr} = 5$ nm, $\theta_{\min} = 0$, $\theta_{\max} = 73.14°$.
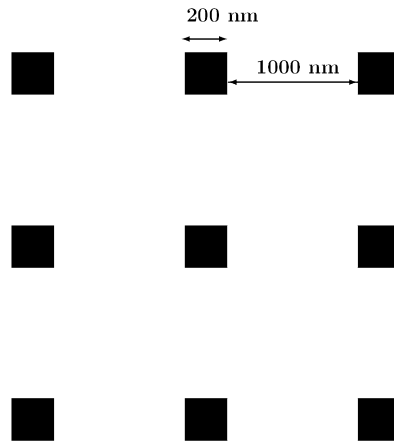

Fig. 8. Sketch of the gold patterned surface prepared by I. Roch Jeune (IEMN). The black squares correspond to the holes where gold has been removed by ion beam etching.

chemical etching. The sample pattern (see Fig. 8) is made by a periodic distribution of squared holes (width 200 nm), where gold has been removed, separated by a distance of 1 µm. In between holes the surface forms gold plateaus.

4.2. SSPM amplitude images

We report in Fig. 9 two sets of images captured on the structured gold sample for **p** (resp. **s**) polarization, on the left (resp. right) column. The images are obtained by scanning the objective in the X, Y directions, for a fixed defocus Z. These amplitude $|V_Z(X,Y)|$ images have been recorded for 5 values of Z, as described in the caption. The grey coding and scale of the images are the same. We note that when the objective lens is focused in the coupling medium (glass) the image contrast of either **p** or **s** polarizations does not change much. However, the holes are detected more clearly for **p** polarization. They are recognizable as small dark rectangles on Fig. 9(b), the center of these small spots is brighter because these points are in anti-phase compared to the edge of the hole. The width of the central grey spot can be compared to the PSF of this microscope (~ 210 nm). For positive values of Z, the contrast of the holes is inverted: for **p** polarization they are very bright and show a double lobe pattern that does not appear in **s** polarization. The **p** polarization images again have a better contrast than the **s** polarization ones. For larger Z values, the $|V(Z)|$ pattern of the gold surface is less immediate to interpret, since diffraction of the hole contours produces geometric forms with a hexagonal symmetry. For the **s** polarization
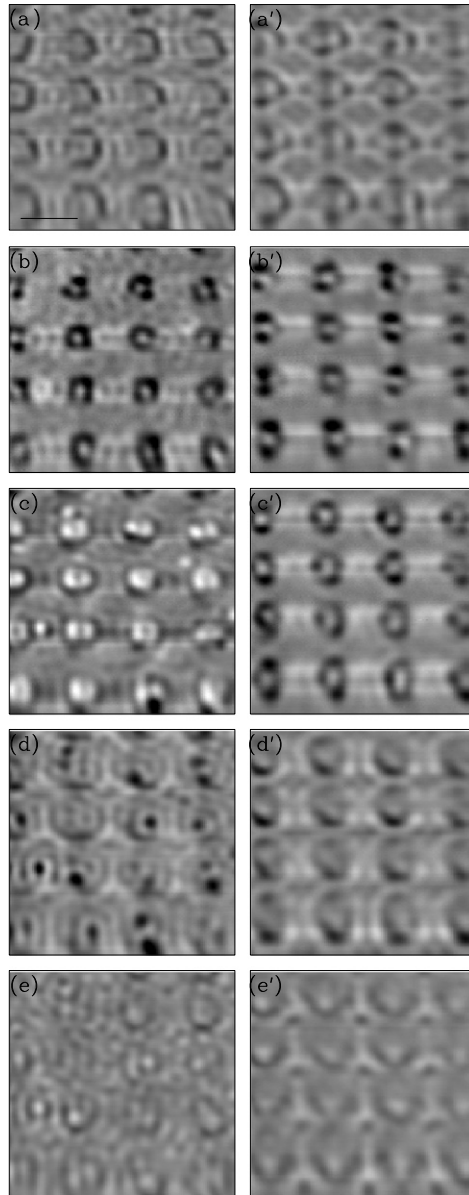
Fig. 9. SSPM images of the structured gold surface. (a) to (e) $|V(Z)|$ in **p** polarization. (a′) to (e′) $|V(Z)|$ in **s** polarization. For both polarizations the Z values are respectively from top to bottom: -0.48 μm, -0.1 μm, 0.3 μm, 0.7 μm and 1.06 μm respectively. $|V(Z)|$ Images are coded in grey from black to white in the range $[-0.12; 0.12]$. Scale (black) bar in (a) is 1 μm.

images, the evolution with Z is simpler: the spot sizes corresponding to gold holes increase progressively and their contrast diminishes.

4.3. $V(Z)$ curves reconstruction

Here we compare both the modulus and the phase of $V(Z)$ curves on two different positions of the surface, respectively inside a hole and on a gold plateau. In each case, we also compare the **p** and **s** polarizations. Figs. 10 and 11 correspond to a gold plateau and a gold hole respectively. The $|V(Z)|$ curves corresponding to a gold plateau (Fig. 10(a)) and to a hole (Fig. 11(a)) for a **p** polarization are easily distinguishable, whereas for a **s** polarization the distinction is not immediate. For **p** polarization, the slow modulations of $|V(Z)|$ $(Z > 0)$ occur on gold plateaus whereas they disappear inside the holes which are empty of gold. This makes sense since these oscillations are the footprint of SPR. The higher contrast of $|V|$ images in (Fig. 9) for positive values of Z (in **p** polarization) is due to surface plasmon enhancement of the electromagnetic field.

We compare in Figs. 10(b) and 11(b) the phase $\Phi_P(Z)$ and $\Phi_S(Z)$ for **p** and **s** polarization respectively. Although for a **p** polarization $\Phi_P(Z)$ curves bear more modulations than $\Phi_S(Z)$ curves, the comparison of these plots is rather difficult.
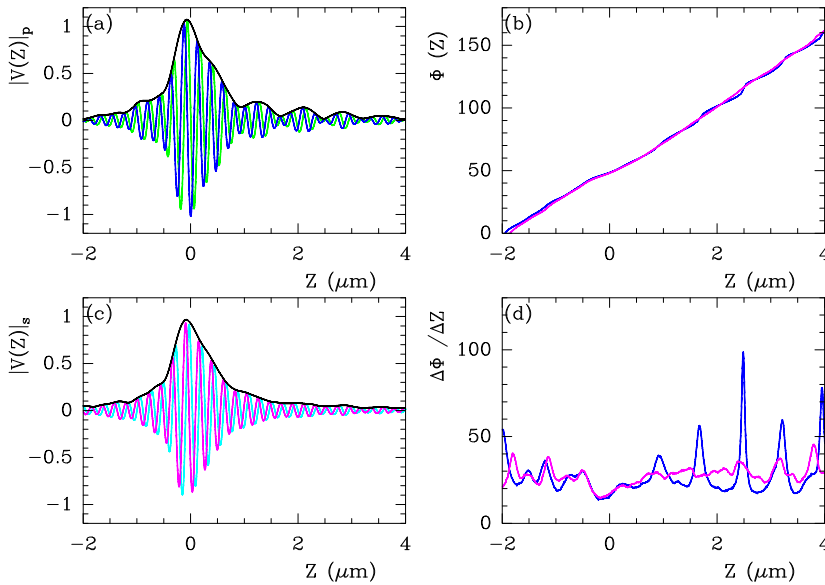
Fig. 10. Experimental $V(Z)$, $\Phi(Z)$ and $\Delta\Phi/\Delta Z$ recorded on a point centered on a gold plateau. (a) $|V(Z)|$ in black, $\Re(V(Z))$ in blue, and $\Im(V(Z))$ in green, recorded in **p** polarization. (b) Comparison of the phases $\Phi(Z)$ in **p** (in blue) and **s** polarization (in magenta). (c) $|V(Z)|$ in black, $\Re(V(Z))$ in cyan, and $\Im(V(Z))$ in magenta, recorded in **s** polarization. (d) Comparison of the Z derivative of the phase $\Delta\Phi/\Delta Z$ in **p** (in blue) and in **s** polarization (in magenta). Each curve corresponds to the average over 10 recordings on the same X, Y point.
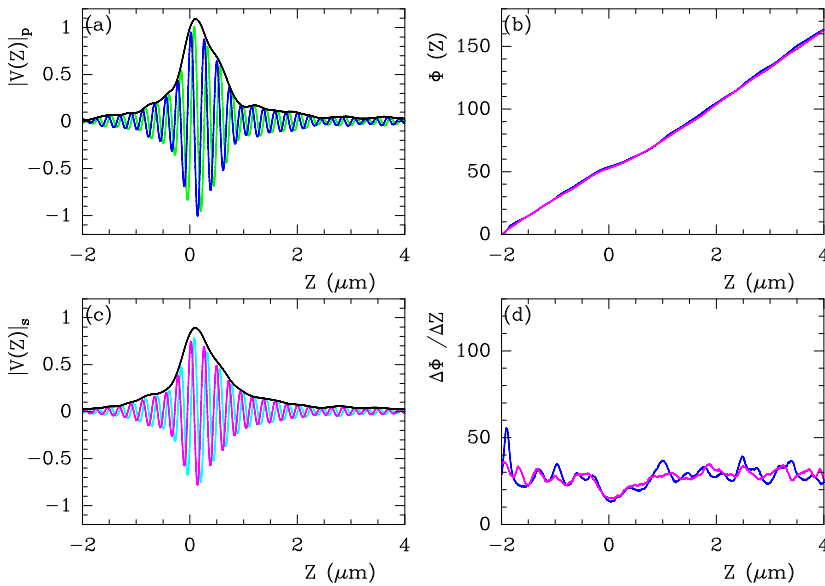

Fig. 11. Experimental $V(Z)$, $\Phi(Z)$ and $\Delta\Phi/\Delta Z$ recorded on a point centered inside a gold hole. (a) $|V(Z)|$ in black, $\Re(V(Z))$ in blue, and $\Im(V(Z))$ in green, recorded in **p** polarization. (b) Comparison of the phases $\Phi(Z)$ in **p** (in blue) and **s** polarization (in magenta). (c) $|V(Z)|$ in black, $\Re(V(Z))$ in cyan, and $\Im(V(Z))$ in magenta, recorded in **s** polarization. (d) Comparison of the Z derivative of the phase $\Delta\Phi/\Delta Z$ in **p** (in blue) and in **s** polarization (in magenta). Each curve corresponds to the average over 10 recordings on the same X, Y point.

The computation of the derivative of the phase versus Z allows a direct differentiation of the situations considered here. For **s** polarization, it is still possible to tell the difference between the gold plateaus and gold holes although the contrast is poorer. For **p** polarization, the difference between the gold plateau and the gold hole is amplified for specific values of the defocus Z, where the phase varies very rapidly with Z.

4.4. Reconstruction of linear sections of $V(X)$ for fixed Z

Before reconstructing two-dimensional phase images, we have scanned the patterned sample along the X direction with a 30 nm step, on a line which intersects the gold holes, keeping Y constant, and at each point of this linear scan we
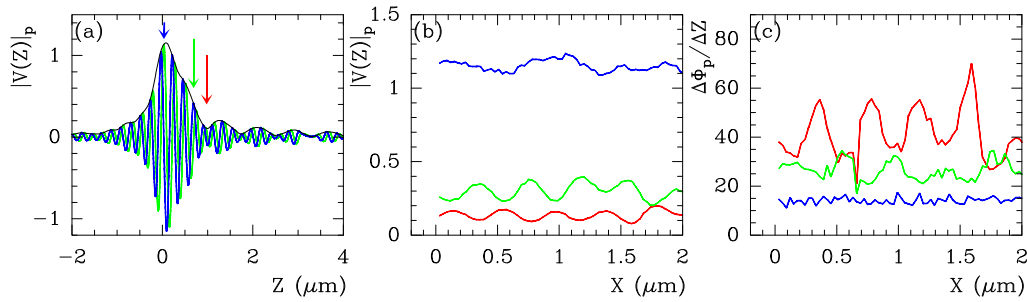
Fig. 12. Modulus and the phase derivative of $V(Z)$ when scanning along the X direction on the patterned surface. (a) $|V(Z)|$ (black), $\Re(V(Z))$ (blue) and $\Im(V(Z))$ (green) on a point located on a gold plateau. (b) Scanned $|V|$ profiles along the X directions, captured for three values of Z, respectively: $Z = 0$ µm (blue profile) (the origin of $V(Z)$ is set at its maximum amplitude), $Z = 0.81$ µm (green profile) and $Z = 1.1$ µm (red profile). (c) $\Delta\phi/\Delta Z$ profiles along the scanning direction X from the same set of data as in (b), same color coding.

have recorded a complete $V(Z)$ curve. We plot in Figs. 12(b) and 12(c) the (one-dimensional) sections of $|V|$ and $\Delta\phi/\Delta Z$ respectively for three defocus Z marked by the colored arrows in Fig. 12(a). For Z close to zero, both amplitude $|V(Z)|$ and phase $\Phi(Z)$ do not show drastic modifications with the lateral position X. For $Z = 0.8$ µm (green curve), $|V|$ increases when the scan crosses a gold hole, as we have already remarked in Fig. 9(c). For a larger Z value ($Z = 1.1$ µm, red curve) $|V|$ is minimum in the gold holes, and maximum on the gold plateaus, its variation is also smaller than for $Z = 0.8$ µm. In Fig. 12(c), we report the variations of $\Delta\Phi/\Delta Z$ along the same X line. We observe that the phase derivative contrast is stronger for $Z = 1.1$ µm than for $Z = 0.8$ µm, in opposition to what was observed on the modulus $|V|$. For these two selected Z values, the red and green scans of $\Delta\Phi/\Delta Z$ are also in antiphase with each other. Moreover the phase derivative variations are larger when the modulus of $V(Z)$ is smaller, which is a reminiscence from the reflectivity curve $r_p(\theta)$ and its argument $\phi_p(\theta)$. This suggests that phase derivative imaging may be better suited for detecting the edge of patterns. The choice of defocus Z corresponding to the extrema of phase derivative will be very important for that purpose. Therefore, it is necessary to acquire successive images using a fine Z sampling.

4.5. Two-dimensional modulus and phase images of V

We illustrate in Fig. 13 the reconstruction of 2D maps of the modulus (panels (a) to (a″)), phase (panels (b) to (b″)) and phase derivative (panels (c) to (c″)) of $V(Z)$. The maximum of contrast depends on the defocus Z, and it is not the same if one considers the modulus or the phase. The contrast of modulus images decreases with the defocus, for better visibility, we therefore adjusted the range of grey coding of the modulus images in this figure. The phase represented in Figs. 13(b) to 13(b″) has been computed with the arctangent method, from the argument of $V(Z)$. A stack of pictures recorded for 130 Z values in the interval $[-1 \text{ µm}, 2 \text{ µm}]$ has been used to reconstruct the full 3D Z-map and to correct the sample tilt [47]. This method compensates surface tilts and allows for a very rigorous scanning of the sample at fixed distance Z to the gold surface. In Figs. 13(c) to 13(c″), the derivative of the phase has been computed for a Z step of 80 nm. In the panels (d) to (d″) we show cross-sections of the images on the left to compare the image contrasts. We observe that both the phase and phase derivative images have a higher contrast at the Z values where $\Delta\Phi/\Delta Z$ is maximum (see the plots of Fig. 10(d)), namely ~ 0.94 µm and ~ 1.66 µm. Moreover the phase difference images gain in contrast for narrow Z intervals corresponding to minima of $|V(Z)|$. We conclude from Fig. 13 that the Z derivation of the phase points out the defocus Z positions where the sensitivity is larger. It is therefore particularly suited for the detection of edges or gradient zones.

5. Conclusion

We have discussed in this manuscript the advantage of phase image uncovering from the reflected field in SSPM, comparatively to amplitude images. The difficulty in phase imaging is the discrimination of the phase variations due to a local index change of the sample from artificial phase variations coming from either mechanical misalignment or electronic noise. To avoid irreversible and time consuming phase detrending and denoising methods, we propose an alternate measure that can be directly extracted from the $V(Z)$ curves provided by the SSPM. This measure corresponds to the angular rotation of the complex vector field $V(Z)$ when Z changes, that we represent as the Z derivative of $\Phi(Z)$. This quantity $\Delta\Phi/\Delta Z$ is very sensitive to local index variations. We have shown from experimental and numerical evidences that $\Delta\Phi/\Delta Z$ can be used instead of $|V|$ to enhance the contrast of the images. Its higher sensitivity to local index defects allows also a higher spatial resolution than that achieved by using the modulus or standard phase computation methods. Despite the fact that the computation of a phase derivative increases the level of noise, this noise does not lead to misinterpretation of the images, because no phase unwrapping is required here. The noise can be filtered afterwards if necessary. A pseudo-analytical demonstration of the interest of this method can be done from the integral equation of $V(Z)$, with simplified expressions of the phase of r_p. The relation between $\Phi(V(Z))$ and $\phi(r_p)$ can also be derived. The first and second order derivatives of $\phi(r_p)$, close to θ_P, can be extracted directly from the $\Delta\Phi/\Delta Z$ curves and used to interpret the modification of the Goos
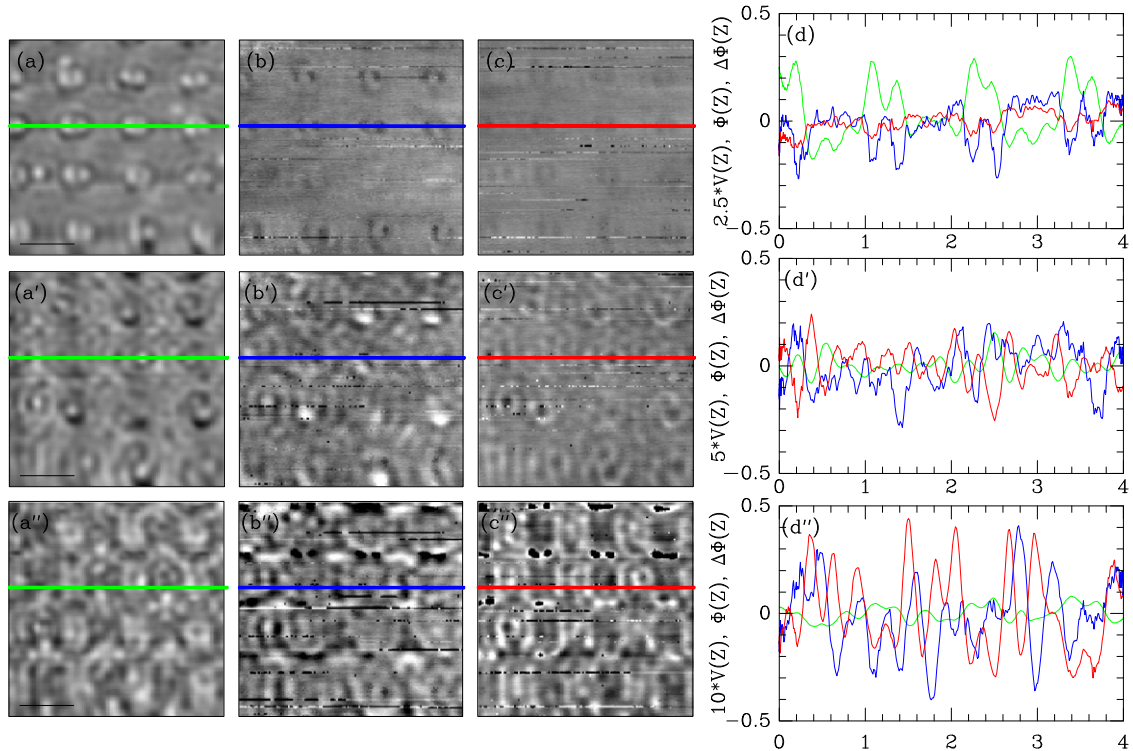
Fig. 13. Left panel: modulus $|V|_I$ (first row), phase Φ_I (second row) and phase derivative $\Delta\Phi_{I,I+1}$ (third row) grey coded pictures recorded from two-dimensional SSPM scans of the gold patterned surface in **p** polarization. Right panel compiles Y sections of the corresponding images. (a) to (d) $Z = 0.24$ μm. (a′) to (d′) $Z = 0.94$ μm, (a″) to (d″) $Z = 1.66$ μm. Phase derivatives has been computed from images with $\Delta Z = 80$ nm. The range of grey coding is $[-0.50.5]$ except for the modulus images which are coded differently for better contrast: (a) $[-0.20.2]$, (a′) $[-0.10.1]$, (a″) $[-0.050.05]$. Scale (black) bars in (a) are 1 μm.

Hanchen effect due to plasmon resonance [48,49]. These computations are currently under progress, on which we plan to elaborate more deeply in a future communication.

Acknowledgements

References

[1] A. Otto, Excitation of nonradiative surface plasma waves in silver by the method of frustrated total reflection, Z. Phys. 216 (1968) 398–410.

[2] H. Raether, Physics of Thin Films, vol. 9, Academic Press, New York, 1977, pp. 145–261 (Chapter III).

[3] J.-D. Swalen, J.-G. Gordon, M.-R. Philpott, A. Brillante, I. Pochrand, R. Santo, Plasmon surface polariton dispersion by direct optical observation, Am. J. Phys. (1980) 669–671.

[4] B.-R. Nelson, T.-E. Grimsrud, M.-R. Liles, R.-M. Goodman, R.-M. Corn, Surface plasmon resonance imaging measurements of DNA and RNA hybridization adsorption onto DNA microarrays, Anal. Chem. 73 (2001) 1–7.

[5] J. Homola, S. Yee, G. Gauglitz, Surface plasmon resonance sensors: review, Sensors and Actuators B 54 (1999) 3–15.

[6] J. Homola, Surface plasmon resonance base sensors, in: O.S. Wolfbeis (Ed.), Springer Ser. Chem. Sens. Biosens., vol. 4, Springer, Berlin/Heidelberg, 2006, pp. 3–44.

[7] F. Abeles, T. Lopez-Rioz, A. Tadjeddine, Investigation of the metal–electrolyte interface using surface plasma waves with ellipsometric detection, Solid State Commun. 16 (1975) 843–847.

[8] S. Nelson, K. Johnston, S. Yee, High sensitivity surface plasmon resonance sensor based on phase detection, Sensors and Actuators B 35–36 (1996) 187–191.

[9] A. Kabashin, P. Nikitin, Surface plasmon resonance interferometer for bio and chemical sensors, Opt. Commun. 150 (1998) 5–8.

[10] P. Nikitin, A. Beloglazov, V. Kochergin, M. Valeiko, T. Ksenevich, Surface plasmon resonance interferometry for biological and chemical sensing, Sensors and Actuators B 54 (1999) 43–50.

[11] V. Kochergin, A. Beloglazov, M. Valeiko, P. Nikitin, Phase properties of a surface-plasmon resonance from the point of view of sensor applications, Quantum Electron. 28 (1998) 444–448.

[12] H. Chiang, J. Lin, R. Chang, S. Su, P. Leung, High resolution angular measurement using surface plasmon resonance via phase interrogation at optimal incident wavelengths, Opt. Lett. 30 (2005) 2727–2729.
[13] H. Chiang, J. Lin, Z. Chen, High sensitivity surface plasmon resonance sensor based on phase interrogation at optimal incident wavelengths, Appl. Phys. Lett. A 88 (2006) 141105.
[14] A. Grigorenko, P. Nikitin, A. Kabashin, Phase jumps and interferometric surface plasmon resonance imaging, Appl. Phys. Lett. 75 (1999) 3917–3919.
[15] A. Notcovich, V. Zhuk, S. Lipson, Surface plasmon resonance phase imaging, Appl. Phys. Lett. 76 (13) (2000) 1665–1667.
[16] P. Dawson, K. Smith, F. de Fornel, J.-P. Goudonnet, Imaging of surface plasmon launch and propagation using a photon scanning tunneling microscope, Ultramicroscopy 57 (1995) 287–292.
[17] P. Dawson, B. Puygranier, J.-P. Goudonnet, Surface plasmon polariton propagation length: a direct comparison using photon scanning tunneling microscopy and attenuated total reflection, Phys. Rev. B 63 (2001) 205410, 10 pp.
[18] A. Grigorenko, A. Beloglazov, P. Nikitin, C. Kuhne, G. Steiner, R. Salzer, Dark-field surface plasmon microscopy, Opt. Commun. 174 (2000) 151–155.
[19] J. Zhang, Q. Dai, G. Wang, Surface plasmon interferometric microscopy for three dimensional imaging of dynamic processes, Opt. Lett. 31 (2006) 3004–3006.
[20] J. Lee, H. Shih, C. Hong, T. Chou, Measurement of refective index change by surface plasmon resonance and phase quadrature interferometry, Opt. Commun. 276 (2007) 283–287.
[21] E. Fu, J. Folay, P. Yager, Wavelength-tunable surface plasmon resonance microscope, Rev. Sci. Instrum. 74 (2003) 3182–3184.
[22] H. Kano, S. Mizuguchi, S. Kawata, Excitation of surface plasmon polaritons by a focused laser beam, J. Opt. Soc. Am. B 15 (4) (1998) 1381–1386.
[23] M.G. Somekh, S.G. Liu, T.S. Velinov, C.W. See, Optical $V(z)$ for high resolution 2π surface plasmon microscopy, Opt. Lett. 25 (11) (2000) 823–825.
[24] M.G. Somekh, S.G. Liu, T.S. Velinov, C.W. See, High resolution scanning surface plasmon microscopy, Appl. Opt. 39 (2000) 6279–6287.
[25] B. Hecht, H. Bielefeldt, L. Novotny, Y. Inouye, D. Pohl, Local excitation, scattering and interference of surface plasmons, Phys. Rev. Lett. 77 (1996) 1889–1992.
[26] A. Bouhelier, F. Ignatovich, A. Bruyant, C. Huang, G.C. des Francs, J.-C. Weeber, A. Dereux, G. Wiederrecht, L. Novotny, Surface plasmon interference excited by tightly focused laser beams, Opt. Lett. 32 (2007) 2535–2537.
[27] M. Somekh, Surface plasmon fluorescence microscopy: an analysis, J. Microsc. 206 (2002) 120–131.
[28] G. Stabler, M. Somekh, C. See, High resolution wide-field surface plasmon microscopy, J. Microsc. 214 (2004) 328–333.
[29] L. Berguiga, S.-J. Zhang, F. Argoul, J. Elezgaray, High-resolution surface-plasmon imaging in air and in water: $V(z)$ curve and operating conditions, Opt. Lett. 32 (5) (2007) 509–511.
[30] B. Huang, F. Yu, R. Zare, Surface plasmon resonance imaging using a high numerical aperture microscope objective, Anal. Chem. 79 (2007) 2979–2983.
[31] K. Watanabe, N. Horiguchi, H. Kano, Optimized measurement probe of the localized surface plasmon microscope by using radially polarized illumination, Appl. Opt. 46 (22) (2007) 4985–4990.
[32] R. Vander, S. Lipson, High resolution surface plasmon resonance real-time imaging, Opt. Lett. 34 (2009) 37–39.
[33] E. Kretschmann, H. Raether, Radiative decay of non radiative surface plasmons excited by light, Z. Naturforsch. A 23 (1968) 2135–2136.
[34] M. Born, E. Wolf, Principles of Optics: Electromagnetic Theory of Propagation, Interference and Diffraction of Light, Cambridge University Press, 1997.
[35] H. Raether, Solid state excitations by electrons (plasma state excitations by electrons), in: Springer Tracts Mod. Phys., vol. 38, 1965, pp. 84–157.
[36] H. Raether, Surface Plasmons on Smooth and Rough Surfaces and on Gratings, Springer Tracts Mod. Phys., vol. 111, Springer, Berlin, 1988.
[37] T. Roland, A. Khalil, A. Tanenbaum, L. Berguiga, P. Delichère, L. Bonneviot, J. Elezgaray, A. Arneodo, F. Argoul, Revisiting the physical processes of vapodeposited thin gold films on chemically modified glass by atomic force and surface plasmon microscopies, Surf. Sci. 603 (22) (2009) 3307–3320.
[38] S. Zhang, L. Berguiga, J. Elezgaray, T. Roland, C. Faivre-Moskalenko, F. Argoul, Surface plasmon resonance characterization of thermally evaporated thin gold films, Surf. Sci. 601 (23) (2007) 5445–5458.
[39] B. Ran, S. Lipson, Comparison between sensitivities of phase and intensity detection in surface plasmon resonance, Opt. Express 14 (2006) 5641–5650.
[40] T. Roland, L. Berguiga, J. Elezgaray, F. Argoul, Scanning surface plasmon imaging of nanoparticles, Phys. Rev. B 81 (23) (2010) 235419.
[41] L. Berguiga, F. Argoul, Microscope de plasmon de surface haute résolution à balayage en interférométrie hétérodyne avec polarisation radiale, CNRS-ENS Lyon patent DI01877-01, 2008.
[42] J. Elezgaray, T. Roland, L. Berguiga, F. Argoul, Modeling of scanning surface plasmon microscope, J. Opt. Soc. Amer. A 27 (3) (2010) 450–457.
[43] A. Atalar, An angular-spectrum approach to contrast in reflection acoustic microscopy, J. Appl. Phys. 40 (1978) 5130–5139.
[44] A. Atalar, A physical model for acoustic signatures, J. Appl. Phys. 50 (1979) 8237–8239.
[45] C. Ilett, M. Somekh, G. Briggs, Acoustic microscopy of elastic discontinuities, Proc. Roy. Soc. Lond. Ser. A 393 (1984) 171–183.
[46] M. Somekh, Surface plasmon and surface wave microscopy, in: P. Torok, F.J. Tao (Eds.), Optical Imaging and Microscopy, in: Springer Ser. Opt. Sci., vol. 87, Springer-Verlag, Berlin/Heidelberg, 2007, pp. 347–399 (Chapter 14).
[47] L. Berguiga, T. Roland, K. Monier, J. Elezgaray, F. Argoul, Amplitude and phase images of cellular structures with a scanning surface plasmon microscope, Opt. Express 19 (2011) 6571–6586.
[48] X. Yin, L. Hesselink, Goos-hanchen shift surface plasmon resonance sensor, Appl. Phys. Lett. 89 (2006) 261108.
[49] J. Jose, F. Segerink, J. Korterik, H. Offerhaus, Near-field observation of spatial phase shifts associated with goos-hanchen and surface plasmon resonance effects, Opt. Express 16 (2008) 1958–1964.